International Journal of Plasticity 169 (2023) 103706

Contents lists available at ScienceDirect

International Journal of Plasticity

journal homepage: www.elsevier.com/locate/ijplas

On the spatio-temporal characteristics of the Portevin-Le Chatelier effect in aluminium alloy AA5182: An experimental and numerical study

Jianbin Xu [a,b,*], Odd Sture Hopperstad [b], Bjørn Holmedal [a], Torodd Berstad [b], Tomáš Mánik [a], Knut Marthinsen [a]

[a] Department of Materials Science and Engineering, Norwegian University of Science and Technology (NTNU), Sem Sælands vei 14, Trondheim NO-7491, Norway

[b] Centre for Advanced Structural Analysis (CASA), Department of Structural Engineering, Norwegian University of Science and Technology (NTNU), Richard Birkelands vei 1a, Trondheim NO-7491, Norway

ARTICLE INFO

Keywords:
Portevin–Le Chatelier effect
Digital image correlation
Spatio-temporal behaviours
Band characteristics
Finite element modelling

ABSTRACT

The Portevin–Le Chatelier (PLC) effect and its spatio-temporal characteristics in the aluminium alloy AA5182 are studied experimentally and numerically in the current work. An extremely high-frequency camera (up to 1000 Hz) is utilized to capture the nucleation and propagation of the PLC bands in uniaxial tension tests with different applied strain rates. The spatio-temporal patterns and the strain accumulation are obtained from digital image correlation (DIC). A transition from continuous to discontinuous band propagation is observed with increasing strain rate. Finite element simulations are carried out using a modified Kubin-Estrin-McCormick (KEMC) model to reproduce the serration morphologies, spatio-temporal patterns and strain accumulation processes. Based on the comparison between experiments and modelling, it is revealed that the strain accumulation and strain ageing processes together decide the subsequent band nucleation. The PLC band inherently brings a strain heterogeneity to the specimen, which results in different levels of work-hardening across the specimen. The strain ageing process, which occurs both inside and outside the PLC band, is found to create another heterogeneity in terms of the solute strengthening. A unique local yield stress minimum leads to a propagating band, while multiple local yield stress minima give a jumping band behaviour. Using that equilibrium forces the work-hardening behind the propagating band to be balanced with the solute strengthening in front of the band, analytical expressions for the band strain and band velocity are derived and verified by the experimental data.

1. Introduction

The PLC effect is a manifestation of dynamic strain ageing (DSA), which is strongly temperature and strain rate dependant (Kabirian et al., 2014; Li et al., 2019; Shen et al., 2020; Wang et al., 2015). The most widely accepted explanation is that the plastic instability leading to the PLC bands stems from the negative strain rate sensitivity of the material (Penning, 1972), i.e., a local strain rate increase will result in a softening of the material. At the microscopic scale, the dislocations move in a stop-and-go manner and the

* Corresponding author.
E-mail address: jianbin.xu@ntnu.no (J. Xu).

https://doi.org/10.1016/j.ijplas.2023.103706
Received 11 June 2023; Received in revised form 12 July 2023;
Available online 17 July 2023

solute diffusion occurs when the dislocations are temporarily arrested (McCormick, 1988). A lower external strain rate usually results in slower dislocation motion, which makes the solute pinning more efficient, and vice versa. The collective dislocation movements determine the macroscopic behaviour of the material (Kubin et al., 2002).

During the tensile deformation, a narrow, inclined propagating band in which the plastic deformation takes place is typically observed, which is similar to the well-known Lüders yield plateau phenomenon (Hallai and Kyriakides, 2013; Wenman and Chard--Tuckey, 2010). However, the PLC bands are nucleating and propagating repeatedly. Three different types of PLC bands are classified based on the spatio-temporal behaviours (De Codes et al., 2011; Halim et al., 2007; Zhang et al., 2005) and the associated serration morphologies of the stress-strain curves (Lebyodkin et al., 2000). At high strain rate, type A serrations with a small amplitude are often observed, and the band travels continuously in a fast sequence. Type B serrations with shorter-distance band propagation compared to type A, occur at intermediate strain rates. At low strain rate, type C serrations with large stress drops and more random band nucleation are obtained. In reality, the band type will vary with the strain level and different band types may coexist in a single test (Ait-Amokhtar and Fressengeas, 2010). More refined band type definitions can be found in Jacobs et al. (2019).

The wave-like bands carry almost all plastic deformation of the specimen. Thus, despite the great differences in the band propagation behaviours and the serration morphologies, both the band speed (type A) and the nucleation frequency (type C) greatly depend on the overall imposed deformation. On the other hand, the internal material properties also play an important role on the band kinematics, especially the work-hardening behaviour of the material, which is directly or indirectly affected by the strain accumulation (Zavattieri et al., 2009), precipitates (Chen et al., 2021), grain size (Yuzbekova et al., 2021, 2017), solute concentration (Kang et al., 2012; Luo et al., 2018), temperature and strain rate (Xu et al., 2022, 2023; Yang et al., 2018). The interplay of the external kinematic boundary conditions and the intrinsic properties of the material significantly complicate the analysis of the band behaviour.

The PLC effect is often characterized by the band velocity v_b, the band strain Δp_b, the band strain rate $\dot{p}_b$ and the band width w_b. With the development of the digital image correlation (DIC) technique, it is now possible to detect the heterogeneous deformation in real-time (Besnard et al., 2006; Lee et al., 2021; Swaminathan et al., 2015). Often, it is thought that the deformation is localized within the band, while almost no plastic deformation takes place outside the band. The band strain rate $\dot{p}_b$ increases with the applied strain rate $\dot{\varepsilon}_a$ and plastic strain accumulation p (Yuzbekova et al., 2017; Zavattieri et al., 2009). Moreover, $\dot{p}_b$ has been found to be dependant on the state of the material, e.g., different initial dislocation densities (Yuzbekova et al., 2017). The band strain Δp_b has been considered to increase as the deformation proceeds (Kang et al., 2012; Ranc and Wagner, 2005), whereas the band velocity v_b has been found to increase with the applied nominal strain rate $\dot{\varepsilon}_a$ (Hähner and Rizzi, 2003; Min et al., 2014; Shabadi et al., 2004), or more precisely to be linearly dependant of $\dot{\varepsilon}_a$ (Mazière et al., 2010). In addition, the band velocity v_b has also been found to decrease with the strain accumulation (Benallal et al., 2008a; Hopperstad et al., 2007; Shabadi et al., 2004), and the band width w_b is considered to be proportional to the thickness of the specimen (Zhang et al., 2005).

Numerical simulations are widely utilized to study the PLC effect, such as the serration morphologies, spatio-temporal patterns and band characteristics. Lebyodkin and co-authors applied a simple spatial coupling model in terms of the local time-dependant stress response to reproduce the different types of serrations (Lebyodkin et al., 2000). Hähner and co-authors proposed a physically based model, of which the activation enthalpy was used as an internal state variable, and a characteristic length scale was introduced for the temporal and spatial coupling. A good qualitative agreement with the experiment has been reached with respect to the spatio-temporal patterns (Hähner and Rizzi, 2003; Hähner et al., 2002; Rizzi and Hähner, 2004). Similar approaches using a finite difference scheme can also be found in other works (Jiang et al., 2007; McCormick and Ling, 1995). A finite element (FE) model was employed by Zhang et al. (2001) to study the PLC band morphologies in an Al–Mg–Si alloy. Based on the work of Kubin and Estrin (Kubin and Estrin, 1990) and McCormick (Kubin and Estrin, 1990; McCormick, 1988), an elastic-viscoplastic FE model was applied to predict the band velocity, band width and strain rate within the PLC band and the results were compared to experimental data (Benallal et al., 2008a, 2008b; Hopperstad et al., 2007; Ren et al., 2021). Due to the local softening mechanism, the dependence of the band characteristics on the mesh size is an important issue (Benallal et al., 2006; Klusemann et al., 2015; Marais et al., 2012) and was systematically investigated by Mazière et al. (2010).

Another remarkable feature of the PLC effect is that the plastic instability emerges only after a certain level of strain, i.e., a "critical strain" is required. With increasing applied strain rate, an increase of the critical strain is observed in the high strain rate range, while a decrease of the critical strain is seen in the low strain rate range (Fu et al., 2012). These observations are known as "normal" and "inverse" critical strain behaviour, respectively. Great efforts have been put on understanding the critical strain behaviour of the PLC effect. A systematic experimental investigation by Mulford and Kocks (1979) showed that the strain rate sensitivity will decrease within the jerky flow domain, while an increasing strain rate sensitivity is observed outside the jerky flow domain. This reveals the intrinsic connections between the PLC effect and negative strain rate sensitivity, i.e., the requirement for PLC effect is $S < 0$, where $S = \partial\sigma/\partial \ln\dot{p}$ is the strain rate sensitivity. By utilizing this criterion, Kubin and Estrin (1990) proposed a consistent explanation for the onset and termination of the jerky flow, where the elementary strain increment Ω is assumed to be non-monotonically strain dependant. The "normal" and "inverse" critical strain behaviours are considered as two specific scenarios for materials exhibiting the PLC effect. Alternatively, instead of changing the monotonicity of Ω, a simple phenomenological constitutive model was then suggested by Böhlke et al. (2009), where the saturation ageing stress is assumed to be strain dependant. With this latter model, good agreement with the experimental results was obtained in terms of the band width, the band velocity and the statistical distribution of the serration amplitudes. Recently, Klusemann et al. (2015) applied this model to simulate the PLC effect, and the correlations between

the serration morphologies and the band kinematics were captured with good accuracy. In the current work, the modifications for the saturation ageing stress as suggested by Böhlke et al. (2009) is also adopted to simulate the PLC effect in the aluminium alloy AA5182.

As shown above, numerous experimental and numerical works have been carried out to detect or predict the spatio-temporal characteristics of the PLC bands. However, in most of the above studies, the emphasis has been on phenomenological aspects, leaving the underlying mechanisms of the spatio-temporal behaviour unclear. The role played by the intrinsic properties of the material and the applied external loading on the nucleation and propagation PLC bands is still not well understood. In this paper, the spatio-temporal behaviour of the PLC bands in the aluminium alloy AA5182 is systematically investigated both experimentally and numerically. While previous studies have shown that several factors, such as the overall strain rate, temperature, strain, and microstructure, are important, a more comprehensive understanding of what fundamentally influences the band characteristics is of considerable interest. Additionally, explicit expressions for band strain and band velocity, derived from stress equilibrium considerations across the bands, are experimentally validated. Given that PLC bands can have adverse effects on structural integrity and reduce the surface finish quality of final products, we believe that a better understanding of the spatio-temporal characteristics of PLC bands can serve as a valuable guide in mitigating the detrimental influences caused by PLC bands.

The present paper is organized as follows. In Section 2, the material and the experiment setup are first described, and then the stress-strain curves for different applied strain rates and the corresponding spatio-temporal characteristics of the PLC bands are presented. In Section 3, the elastic-viscoplastic model employed in this work is presented in detail, including the calibration approach used to identify the model parameters. The simulated and experimental results are then compared and discussed in Section 4. Special attention is given to the spatial-temporal behaviour of the PLC bands, and the factors that control the band characteristics. Based on the simulation results, a systematic investigation of the band strain and the band velocity is carried out. By utilizing a new method for post-processing of DIC data, analytical expressions for the band strain and the band velocity are verified by the experimental results. Conclusions are finally presented in Section 5.

2. Experimental study

2.1. Material and specimen geometry

The material used in this study is a commercial aluminium alloy AA5182-O with alloying elements: Mg (4.55 wt.%), Mn (0.27 wt.%), Fe (0.21 wt.%), Si (0.11 wt.%), Cu (0.0215 wt.%), Ti (0.01 wt.%), Zn (0.005 wt.%) and Cr (0.0033 wt.%). The 1.2 mm-thickness sheet is produced by casting, hot and cold rolling, and subsequent annealing procedures. The material in its final state exhibits a weakly textured microstructure and the average grain size is about 11 μm. Dog-bone shaped specimens were cut by electrical discharge machining with the tensile axis in the rolling direction. The specimen geometry is shown in Fig. 1. Uniaxial tension tests at room temperature were carried out by using a servo-hydraulic 100 kN MTS testing machine.

2.2. Tension test with digital image correlation

In the uniaxial tension test, constant crosshead velocity is applied with the nominal strain rate ranging from 10^{-5} s^{-1} to 1 s^{-1}. As the deformation proceeds, a digital image correlation (DIC) system developed by Fagerholt (2012) is utilized to characterize the heterogeneous deformation of the specimen. To track the local displacement, the samples are pre-painted white and then sprayed with artificial black speckle patterns. A high-speed CCD camera with the resolution of 1397 dpi is used to monitor the deformation process. The acquisition frequency varies from 1 frame/s to 1000 frames/s for tests at different strain rates. At a low strain rate, e.g., $\leq 10^{-1}$ s^{-1}, the camera image covers the entire specimen. However, at a very high strain rate, e.g., 1 s^{-1}, only a narrow strip along the central axis is covered by the camera, instead of the whole specimen, due to the very limited duration of the tests. This method can significantly reduce the storage size of the image and thus ensure an extremely high acquisition frequency. The force signals from the machine and the images taken by the camera are synchronized by the software. A 60-mm virtual extensometer along the central tensile axis of the specimen is also defined, which facilitates the measurement of the global and local strains within the gauge area.

2.3. Stress-strain curves

By using the force signals from the testing machine and the elongation measured by the virtual extensometer, the global true stress-strain curves at different applied strain rates are shown in Fig. 2. The yield stress is about 137 MPa and shows a negligible dependence on the testing conditions. The stress level increases with decreasing strain rate, i.e., negative strain rate sensitivity is observed. Serrated yielding is observed for all the tests except the one at 10^{-5} s^{-1}. The serration amplitude increases with decreasing strain rate. The test

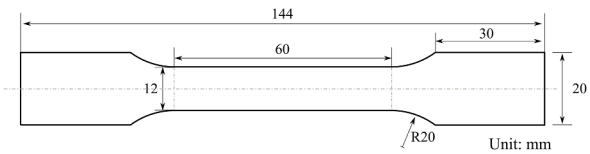

Fig. 1. Specimen geometry of the uniaxial tension test. Using DIC, a 60-mm virtual extensometer is defined along the central axis in the gauge area.

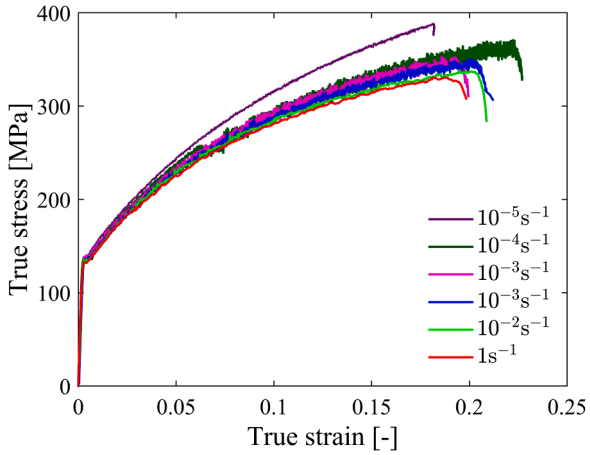

Fig. 2. Experimental true stress-strain curves at room temperature with applied strain rates between 10^{-5} s^{-1} and 1 s^{-1}.

at 1 s^{-1} shows some dynamic effects within 2% strain due to the high applied strain rate, and the stress-strain curve was therefore smoothed. A significant stress increase is observed when the strain rate is lowered from 10^{-4} s^{-1} to 10^{-5} s^{-1}, which is linked to the vanishing of the PLC effect. With the help of the DIC technique, careful checking of each sample's deformation field reveals that all of them experienced the PLC effect, except the one deformed at 10^{-5} s^{-1}.

2.4. Spatial-temporal behaviour of the PLC bands

A convenient way to visualize the band nucleation and propagation is to calculate the strain-rate distribution throughout the test. The strain rate $\dot{\varepsilon}_{xx}$ for each frame is calculated by using the time derivative of the strain increment between two consecutive images, see Zavattieri et al. (2009) and Jacobs et al. (2019) for a more detailed description. The strain measure utilized here is the logarithmic strain ε_{xx} along the tensile direction. Fig. 3 shows the spatio-temporal patterns along with the corresponding stress-strain curves at different strain rates. The intensity of the localization is represented by the colormaps. Both the spatio-temporal pattern and serration morphology exhibit strong dependences on the applied strain rate.

Overall, the PLC band shows a transition from continuous to discontinuous propagation as the strain rate decreases. At the higher strain rates in Fig. 3a-c, it is found that the critical strain decreases with decreasing strain rate, i.e., the "normal" critical strain behaviour. In contrast, the critical strain increases with decreasing strain rate, i.e., the "inverse" critical strain behaviour, for the lower strain rates in Fig. 3d-e. Besides, it is found that $\dot{p}_b$ and w_b both increase with the applied strain rate, which is consistent with the earlier work (Ait-Amokhtar et al., 2006). Based on the spatio-temporal patterns, v_b is found to decrease with strain accumulation.

At 1 s^{-1} in Fig. 3a, light strain-rate fluctuations are first observed around 0.12 s. Afterwards, a well-defined band is seen after 0.15 s. However, it is observed that the propagation of the bands at this stage is not very continuous. This behaviour can likely be attributed to the initial state of the specimen, including factors such as surface roughness and microstructure heterogeneity. Additionally, the proximity to the upper strain-rate limit of the PLC domain could also contribute to this observation. Finally, a continuously propagating type A band is observed before necking starts. As for the tests at $10^{-1}s^{-1}$ and $10^{-2}s^{-1}$ in Fig. 3b-c, type $A + B$ bands are seen, where the band propagates continuously from one end of the specimen to the other (type A), but also with some intermittent short-distance propagation (type B). At strain rates $10^{-3}s^{-1}$ and $10^{-4}s^{-1}$, the band nucleation becomes more random, which is the characteristic of type C bands, see Fig. 3d-e.

3. Numerical study

3.1. Constitutive model

The most widely used constitutive model in simulating the PLC effect is the KEMC model, which is based on the work of Kubin and Estrin (1990) (KE) and McCormick (1988) (MC). Applications of the KEMC model, or modified versions of it, can be found in several works (Benallal et al., 2008a; Böhlke et al., 2009; Hopperstad et al., 2007; Klusemann et al., 2015; Ren et al., 2017; Zhang et al., 2001). As mentioned above, Böhlke et al. (2009) proposed a modified KEMC model, which assumes that the saturation ageing stress due to DSA is linearly dependant on the accumulated plastic strain. This modification of the KEMC model is adopted here.

A constitutive model is developed using a hypoelastic-viscoplasticity framework, where the elastic strains are considered infinitesimal, while the plastic strains and the rotations are allowed to be finite (Belytschko et al., 2013). The rate-of-deformation tensor can be split into elastic and plastic parts,

$$\mathbf{D} = \mathbf{D}^{e} + \mathbf{D}^{p} \tag{1}$$

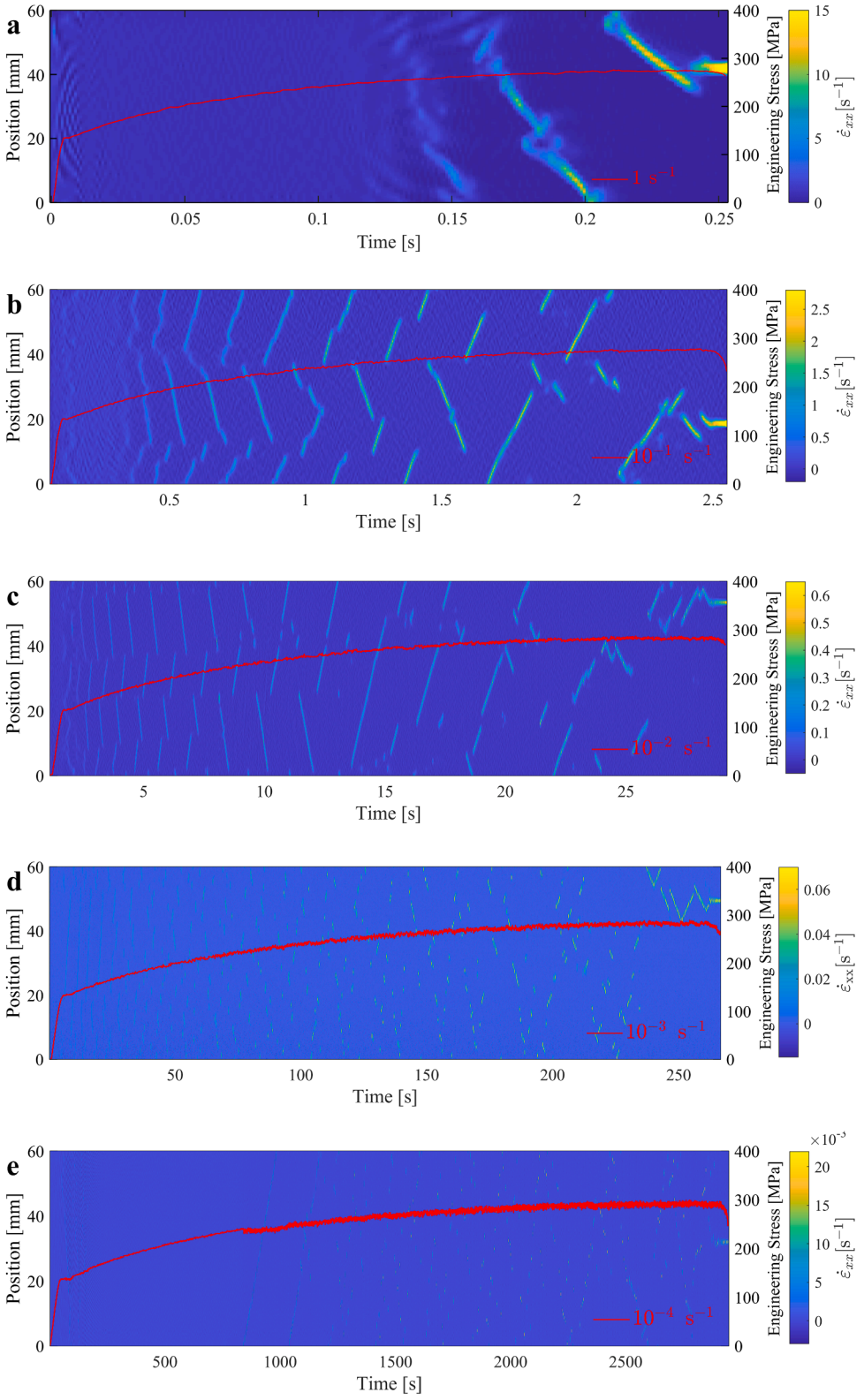

Fig. 3. Local strain rate as a function of position along the centreline of the gauge length and time (or test duration) for applied strain rates: (a) 1 s^{-1}; (b) $10^{-1}s^{-1}$; (c) $10^{-2}s^{-1}$; (d) $10^{-3}s^{-1}$; (e) $10^{-4}s^{-1}$. The red lines denote the corresponding engineering stress-strain curves.

where $\mathbf{D}^{\mathrm{e}}$ and $\mathbf{D}^{\mathrm{p}}$ are the elastic and plastic rate-of-deformation tensors, respectively. The objective Jaumann stress rate $\boldsymbol{\sigma}^{\nabla \mathrm{J}}$ is used here, and the hypoelastic relation is expressed as

$$\boldsymbol{\sigma}^{\nabla \mathrm{J}} \equiv \dot{\boldsymbol{\sigma}} - \mathbf{W}\cdot\boldsymbol{\sigma} - \boldsymbol{\sigma}\cdot\mathbf{W}^{\mathrm{T}} = \left(K - \frac{2}{3}G\right)\mathrm{tr}(\mathbf{D}^{\mathrm{e}})\mathbf{1} + 2G\mathbf{D}^{\mathrm{e}} \tag{2}$$

where, $\dot{\boldsymbol{\sigma}}$ is the material time derivative of the Cauchy stress, $\mathbf{W}$ is the spin tensor, K and G are the shear and bulk moduli, and $\mathbf{1}$ is the second order unit tensor. The von-Mises yield function with isotropic hardening is adopted here,

$$f(\boldsymbol{\sigma},\ p,\ t_{\mathrm{a}}) = \sigma_{\mathrm{eq}}(\boldsymbol{\sigma}) - \sigma_{\mathrm{Y}}(p, t_{\mathrm{a}}) = \sigma_{\mathrm{eq}}(\boldsymbol{\sigma}) - \sigma_0 - R(p) - \sigma_{\mathrm{a}}(t_{\mathrm{a}}) \tag{3}$$

where, σ_{Y} is the threshold for yielding, which is the sum of the initial yield stress σ_0, the work hardening stress R, and the ageing stress σ_{a}. The von Mises equivalent stress σ_{eq} is given by,

$$\sigma_{\mathrm{eq}}(\boldsymbol{\sigma}) = \sqrt{\frac{3}{2}\boldsymbol{\sigma}' : \boldsymbol{\sigma}'} \tag{4}$$

where $\boldsymbol{\sigma}' = \boldsymbol{\sigma} - \frac{1}{3}\mathrm{tr}(\boldsymbol{\sigma})\mathbf{1}$ is the deviatoric stress tensor.

The plastic rate-of-deformation $\mathbf{D}^{\mathrm{p}}$ is defined by the associated flow rule

$$\mathbf{D}^{\mathrm{p}} = \dot{p}\frac{\partial f}{\partial \boldsymbol{\sigma}} = \dot{p}\frac{3}{2}\frac{\boldsymbol{\sigma}'}{\sigma_{\mathrm{eq}}} \tag{5}$$

where the effective plastic strain rate is given by

$$\dot{p} = \begin{cases} 0 & \text{if} \quad f \le 0 \\ \dot{p}_0\left(\dfrac{f}{\sigma_{\mathrm{D}}}\right)^m & \text{if} \quad f > 0 \end{cases} \tag{6}$$

Here, $\dot{p}_0$ is a reference strain rate and σ_{D} and m are parameters governing the instantaneous rate sensitivity of the material. The viscous stress is then obtained as,

$$R_{\mathrm{v}}(\dot{p}) = f = \sigma_{\mathrm{D}}\left(\frac{\dot{p}}{\dot{p}_0}\right)^{1/\mathrm{m}} \tag{7}$$

Based on Eq. (3) and Eq. (7), the viscoplastic constitutive relation becomes,

$$\sigma_{\mathrm{eq}} = \sigma_0 + R(p) + \sigma_{\mathrm{a}}(t_{\mathrm{a}}) + R_{\mathrm{v}}(\dot{p}) \tag{8}$$

A Voce hardening rule is utilized to describe the work hardening stress R, which is a function of the equivalent plastic strain p,

$$R(p) = Q_{\mathrm{R}}(1 - \exp(-C_{\mathrm{R}}p)) \tag{9}$$

where Q_{R} and C_{R} are the work hardening parameters. The ageing stress σ_{a} represents the additional solute strengthening from the dynamically diffused atoms. An expression for the ageing stress σ_{a} was first given by Cottrell and Bilby (1949), and later modified by Louat (1981):

$$\sigma_{\mathrm{a}}(t_{\mathrm{a}}) = \sigma_{\mathrm{a0}}\ c(t_{\mathrm{a}}) = \sigma_{\mathrm{a0}}\left(1 - \exp\left(-\left(\frac{t_{\mathrm{a}}}{t_{\mathrm{d}}}\right)^n\right)\right) \tag{10}$$

where c is the relative effective solute concentration, t_{a} and t_{d} are the ageing time and the characteristic diffusion time, respectively, n is a diffusion-related exponent, and σ_{a0} is the saturation ageing stress. When the dislocations are fully pinned, i.e., $c = 1$, the ageing stress reaches its maximum value. As suggested by Böhlke et al. (2009), this saturation stress term is modified to be strain dependant in order to simulate the "normal" and "inverse" critical strain behaviours,

$$\sigma_{\mathrm{a0}} = \sigma_{\mathrm{a00}} + \acute{\sigma}_{\mathrm{a0}}\ p \tag{11}$$

where σ_{a00} is the initial saturation ageing stress and $\acute{\sigma}_{\mathrm{a0}}$ is the rate of change of the saturation ageing stress with plastic strain. At constant plastic strain rate, or the so-called "steady state", the ageing time equals the average waiting time $t_{\mathrm{a,ss}}$ that the dislocations spend when they are temporally arrested. As for the case of a sudden plastic strain rate change, a relaxation function is proposed by McCormick (1988) to calculate the ageing time transient,

$$\dot{t}_{\mathrm{a}} = 1 - \frac{t_{\mathrm{a}}}{t_{\mathrm{a,ss}}}; \quad t_{\mathrm{a,ss}} = \frac{\Omega}{\dot{p}} \tag{12}$$

In a steady state, the ageing time is inversely proportional to the plastic strain rate. A lower plastic strain rate enables longer ageing

time and thus more efficient solute pinning. As for a non-steady state, the waiting time $t_{a,ss}$ in the new steady state acts as a target for the ageing time t_a evolution (McCormick, 1988). The elementary strain increment Ω is assumed to be linearly dependant on the plastic strain accumulation (Böhlke et al., 2009),

$$\Omega(p) = \Omega_0 + \Omega' p \tag{13}$$

where Ω_0 is the initial value of the elementary strain increment and Ω' is rate of change of Ω with respect to the plastic strain. It should be stated that the evolution of elementary strain increment is still a topic of debate (Kobelev et al., 2017), and in the current work, the linear assumption is primarily employed for the sake of numerical simplicity.

The constitutive model described above has been implemented using a user-defined subroutine (UMAT) for the implicit solver of commercial FEM package Abaqus using a radial return algorithm with consistent tangent operator, cf. Benallal et al. (2008a).

3.2. Finite element model

The tensile tests are simulated in Abaqus/Standard using the constitutive model described in the previous section within the updated Lagrange formulation. Linear solid elements with full integration are utilized for the discretization of the dog-bone shaped tensile specimens in all the simulations, see Fig. 4. Finer elements with in-plane size of 0.6 mm × 0.6 mm are applied in the gauge area, while 4 layers of elements are included in the thickness direction. The left edge of the sample is fixed, while a constant velocity is prescribed on the right edge.

3.3. Parameter identification

The parameter identification is based on the comparison between results from simulations with the constitutive model and the experimental data. As finite element simulations are time consuming, a 1D analytical solution, valid for steady states that neglects the elastic behaviour, was implemented in MATLAB. According to Eqns. (7-13), the flow stress in a steady state can be expressed by

$$\sigma(p,\ \dot{p}) = \sigma_0 + Q_R(1 - \exp(-C_R p)) + \sigma_{a0}(p)\left[1 - \exp\left\{1 - \left(\frac{\Omega(p)}{\dot{p} t_d}\right)^n\right\}\right] + \sigma_D\left(\frac{\dot{p}}{\dot{p}_0}\right)^{1/m} \tag{14}$$

By fitting this equation to the experimental stress-strain curves, initial values of the model parameters are obtained, which will then be taken as the starting values in the finite element simulations. However, the experimental stress-strain curves shown in Fig. 2 are serrated and cannot be directly used to identify the parameters in Eq. (14). Thus, smooth curves are fitted to the experimental stress-strain curves. Owing to the different serration morphologies at different strain rates, the upper envelope of the serrated stress-strain curves is used to fit the smooth curve for tests at the low strain rates, while a standard least squares fitting approach is applied for tests at the intermediate and high strain rates. Discrete datapoints shown in Fig. 5 were obtained from the fitted smooth curves and used as target points in the optimization of the model parameters.

Since the PLC bands lead to a highly heterogeneous deformation field, the 1D solution merely coincides with the stress-strain responses before the onset of serrations. A significant decrease of the average work hardening is observed in the tests exhibiting the PLC effect compared with the test at a strain rate of 10^{-5} s^{-1}, which showed no signs of the PLC effect. Therefore, for tests with strong serrations, i.e., the tests at strain rate $10^{-3}s^{-1}$ and $10^{-4}s^{-1}$, only the part of the stress-strain curve below the critical strain is used in the parameter identification. A least-squares optimization approach was then applied to minimize the difference between the simulated and experimental flow stress. Upper and lower limits of the dynamic ageing parameters were set to match the PLC domain observed experimentally. An initial estimate of the parameter set was thus obtained. In addition, the instability criterion proposed by Mazière and Dierke (2012) were used to carefully adjust the parameters governing DSA. The values of the identified parameters are listed in Table 1.

The results obtained with the fitted 1D analytical solution for steady state are shown in Fig. 5. The stress-strain curves with light serrations in the experiments, i.e., at strain rate $1s^{-1}$, $10^{-1}s^{-1}$ and $10^{-2}s^{-1}$, are perfectly fitted throughout the deformation. The stress-

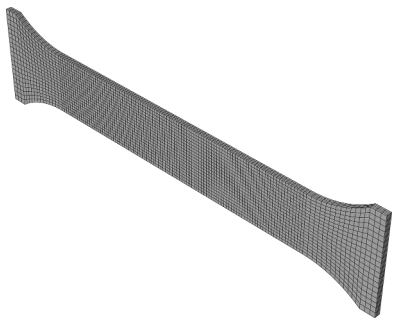

Fig. 4. Finite element model used in the simulations.

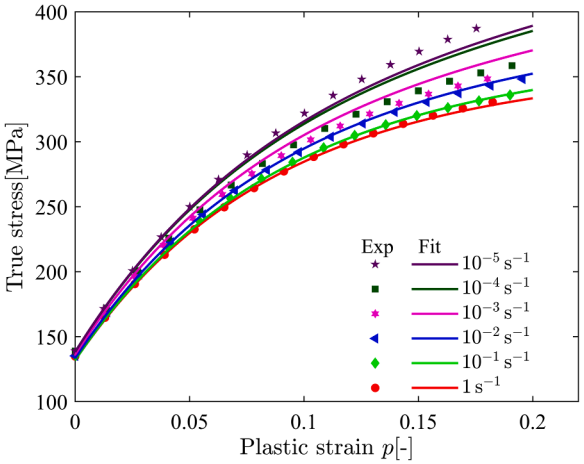

Fig. 5. Parameter identification by fitting the steady-state flow stress curve to the experimental data. Dots denote the experimental datapoints and solid lines represent the fitted steady-state flow stress curve.

Table 1
Parameters for constitutive model.

Symbol	Name	Unit	Value	Equation
$\dot{p}_0$	reference strain rate	1/s	10^{-5}	(7)
σ_D	coefficient in the viscous stress relation	MPa	15	(7)
m	exponent of the viscous stress relation	–	28	(7)
σ_0	initial work hardening stress	MPa	107.5	(8)
Q_R	hardening parameter	–	215.3	(9)
C_R	hardening parameter	–	11.87	(9)
t_d	characteristic diffusion time	s	0.25	(10)
n	diffusion exponent	–	1/3	(10)
σ_{a00}	initial ageing saturation stress	MPa	15.8	(11)
$\sigma_{a0}^{'}$	rate of change of saturation ageing stress	MPa	280	(11)
Ω_0	initial elementary incremental strain	–	4×10^{-4}	(13)
$\Omega^{'}$	rate of change of elementary incremental strain	–	1×10^{-4}	(13)

strain curves with strong serrations in the experiment, i.e., at strain rates $10^{-3}s^{-1}$ and $10^{-4}s^{-1}$, show a good agreement before the onset of serrations. Outside the PLC domain, i.e., at a strain rate 10^{-5} s^{-1}, the flow stress in the late stage is slightly underestimated but still with an acceptable accuracy. The separate contributions from different stress components at 2% plastic strain are shown in Fig. 6. While the work hardening stress is rate independent, the viscous stress increases with the plastic strain rate due to the positive instantaneous strain rate sensitivity. In contrast, the ageing stress decreases with the plastic strain rate, since the ageing time decreases

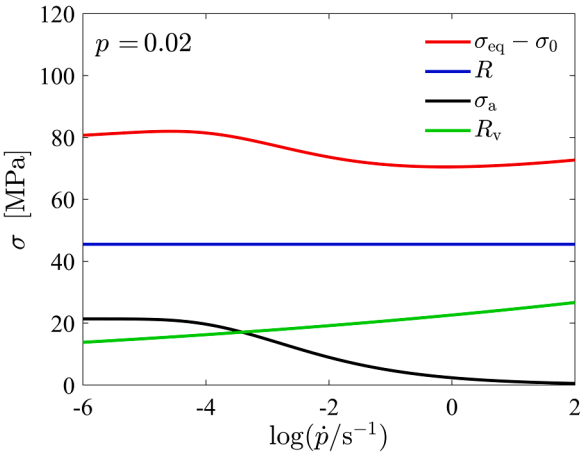

Fig. 6. Stress components vs plastic strain rate at 2% plastic strain.

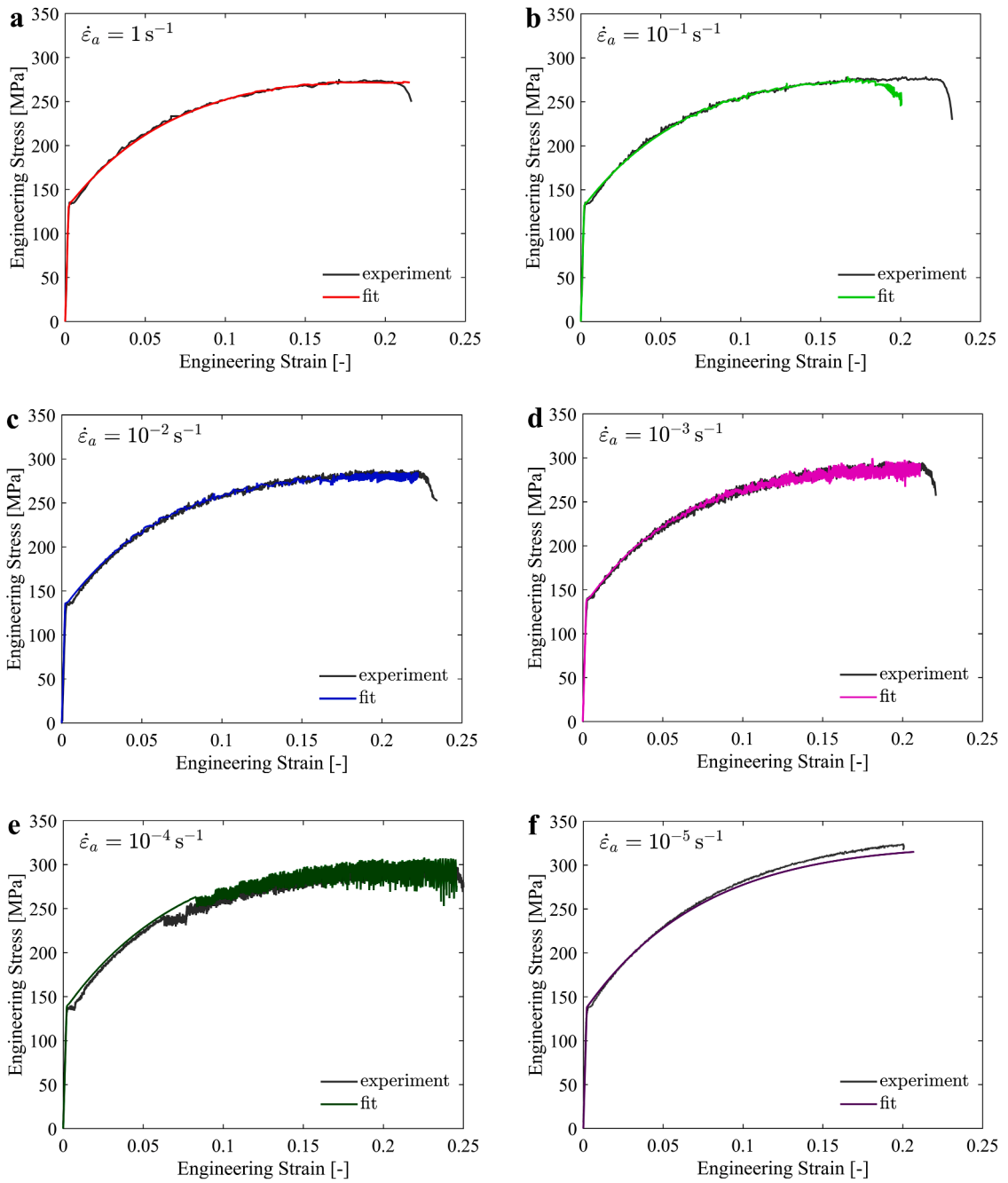

Fig. 7. Comparison between the experimental (lines in grey) and the engineering stress-strain curves obtained in the FE simulations with the identified constitutive model (lines in colour).

with increasing plastic strain rate, and the maximum and minimum values refer to the "fully-aged" and "un-aged" states, respectively. The sum of these three stress components gives a typical "N-shaped" curve associated with the PLC effect as described by (Penning, 1972).

3.4. Finite element simulations

The identified parameters are used as input for the finite element simulations. The simulated and experimental stress-strain curves are shown in Fig. 7. An overall good agreement is found. At strain rates $1s^{-1}$, $10^{-1}s^{-1}$ and $10^{-2}s^{-1}$, the experimental stress-strain curves are perfectly reproduced in the simulations. Also, for the curves with strong serrations, i.e., at strain rates $10^{-3}s^{-1}$ and $10^{-4}s^{-1}$, the overall agreement is good, but the serration amplitudes are overestimated. At strain rate 10^{-5} s^{-1}, the calculated stress-strain curve is serration free, which agrees with the experiment, and no signs of PLC bands are seen in the simulation. However, the stress is slightly underestimated towards necking.

As seen in the experimental results in Fig. 2, the stress level at the lowest strain rate (10^{-5} s^{-1}) is considerably higher than the stress level at the higher strain rates where the PLC effect is present. Reproducing the stress-strain curve with strain rate 10^{-5} s^{-1} in the simulations is pivotal, since it represents the lower boundary of the PLC domain and provides a "baseline" for determining the parameters governing the DSA phenomenon. To capture this behaviour in the simulations, it is necessary to increase the value of σ'_{a0} in Eq. (12), which results in the overestimation of the serration amplitudes. This is the weakest part of the predictions by the current model. As is shown in previous studies (Ren et al., 2017; Xu et al., 2022), solute atoms plays an important role for dynamic recovery and thus for the work hardening behaviour. For the test at the lowest strain rate, the dislocations are fully saturated, which will cause a stronger suppression of the dynamic recovery than at higher strain rates.

Previous studies have shown that FE simulations of the PLC effect are mesh sensitive due to the localization of deformation in the propagating PLC bands induced by the negative strain rate sensitivity (Benallal et al., 2006). As a result, a mesh sensitivity study has been carried out, where the influence of the mesh size on the PLC band characteristics is investigated. The simulated band characteristics with different mesh sizes at 18% global strain are shown in Fig. 8, where each parameter has been normalized by its value at the minimum mesh size. The following band parameters are considered: the band width, w_b, the inverse peak plastic strain rate inside the PLC band, $\dot{p}^{-1}_{b,max}$, the band velocity, v_b, and the band strain, Δp_b. The band width w_b in the axial direction is defined by a plastic strain rate is higher than 0.1 $\dot{p}_{b,\ max}$. It is seen that the band strain rate and band width are mesh sensitive, while the band speed and band strain are independent of the mesh size. Similar results have also been reported in the work of Mazière et al. (2010) and Manach et al. (2014), in which the mesh sensitivity studies were carried out for the McCormick's model (Zhang et al., 2001). It should be noted that non-local approach could be employed to address this issue, however, their impact on the spatio-temporal characteristics appears to be minor for the current research.

4. Results and discussion

4.1. Simulated spatial-temporal patterns

Fig. 9 shows the simulated spatial-temporal patterns at different applied strain rates. The tests at nominal strain rates of 1 s^{-1}, $10^{-2}s^{-1}$ and $10^{-4}s^{-1}$ are selected to illustrate the different band types. All simulations are performed with the same mesh size. The strain rate distribution along the 60 mm gauge is directly exported from the Gauss integration points of the elements. As the applied

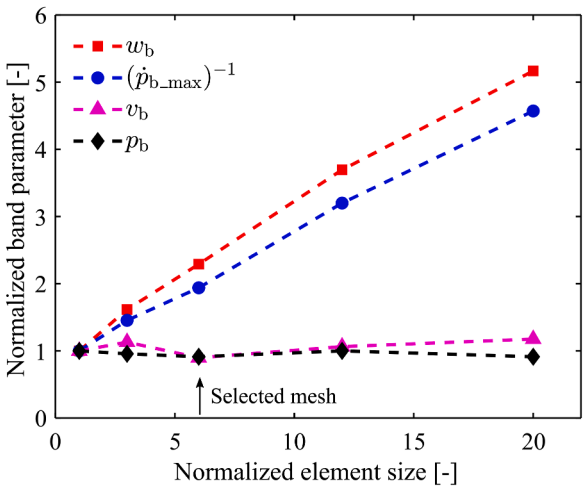

Fig. 8. Simulated band characteristics (normalized) for different mesh sizes.

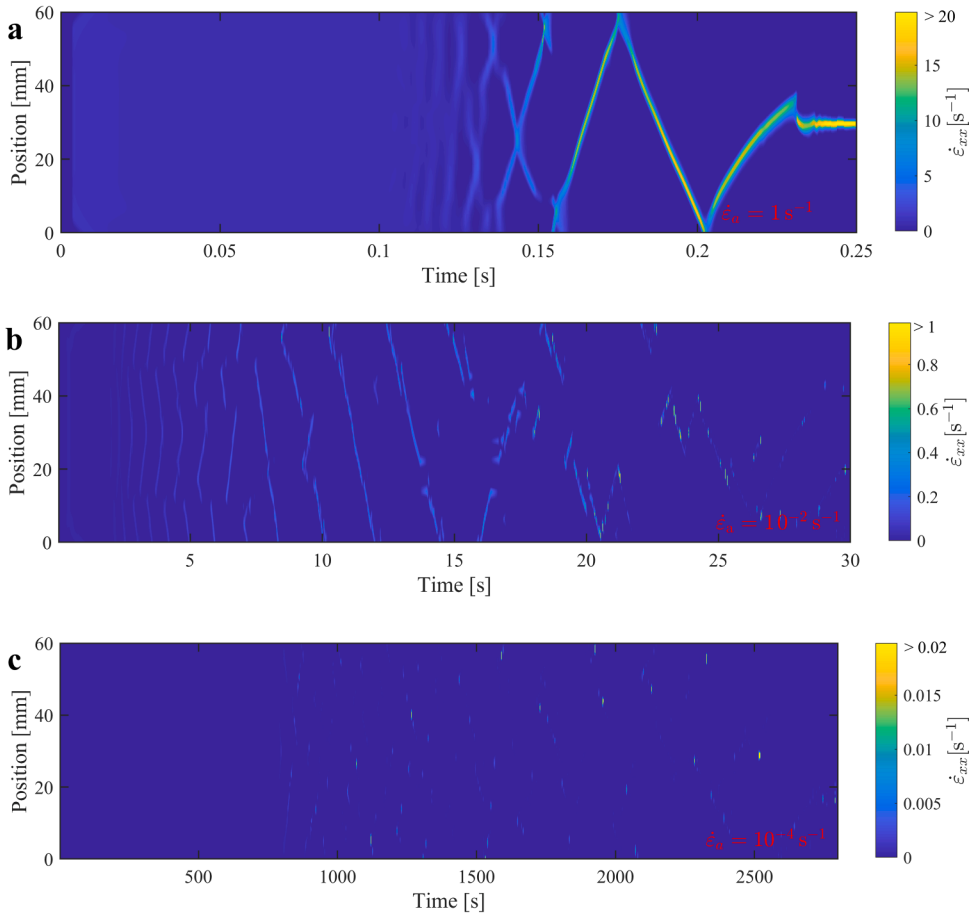

Fig. 9. Simulated spatial-temporal patterns at different strain rates: (a) 1 s^{-1}; (b) $10^{-2}s^{-1}$; (c) $10^{-4}s^{-1}$.

strain rate is increased, the transition from continuous to discontinuous band propagation, as shown in Fig. 3, is well reproduced in the finite element simulations. It should be noted that the exact band position at a given time will change with the mesh size, as reported by Mazière et al. (2010). Moreover, the time increment settings also influence the band positions. Numerical tests have been conducted to study this influence, but the results are deemed outside the scope of this work and are not presented. Although the local strain rate fluctuations bring some uncertainties to the spatio-temporal patterns, the continuous or discontinuous nature of the band propagation is quite stable.

At a high strain rate (1 s^{-1}), the light strain rate fluctuations first seen after 0.1 s in Fig. 9a, agrees quite well with the experiment in Fig. 3a. Afterwards, two bands are simultaneously nucleated and propagating in the opposite direction. After 0.15 s, a well-defined single band is seen both from experiment and simulation. The band is nucleated nearby the grip end and then sweeps across the specimen. The simulated band propagation is quite smooth; however, some irregular intervals are seen in the experimental band propagation during this stage. This is probably because the material in reality is not defect-free, and the roughness of the specimen is not evenly distributed. With further deformation, the strain localization becomes even more pronounced, and after 0.2 s a continuously propagating band appears and remains until necking.

At the intermediate strain rate ($10^{-2}s^{-1}$), the band is less continuous compared to the test at the highest strain rate (1 s^{-1}). In the early stage of deformation, the material exhibits a typical $A + B$ band behaviour, where the band travels continuously but also with some short-distance propagation, see Fig. 9b. The band rarely appears at the same position within each individual band sequence. With strain accumulation, the bands become more randomly nucleated and stationary. Instead of being relatively regular and periodic, the band position is sometimes overlapped even within the same band sequence after 15 s. The simulation is in excellent agreement with the experimental findings and the transition of the band behaviour is well captured.

At a low strain rate of $10^{-4}s^{-1}$, the band nucleation becomes even more random than at the intermediate strain rate ($10^{-2}s^{-1}$), see Fig. 9c. The first band appears at approximate 800 s, which matches the experimental observation in Fig. 3e. In the experiment, the first

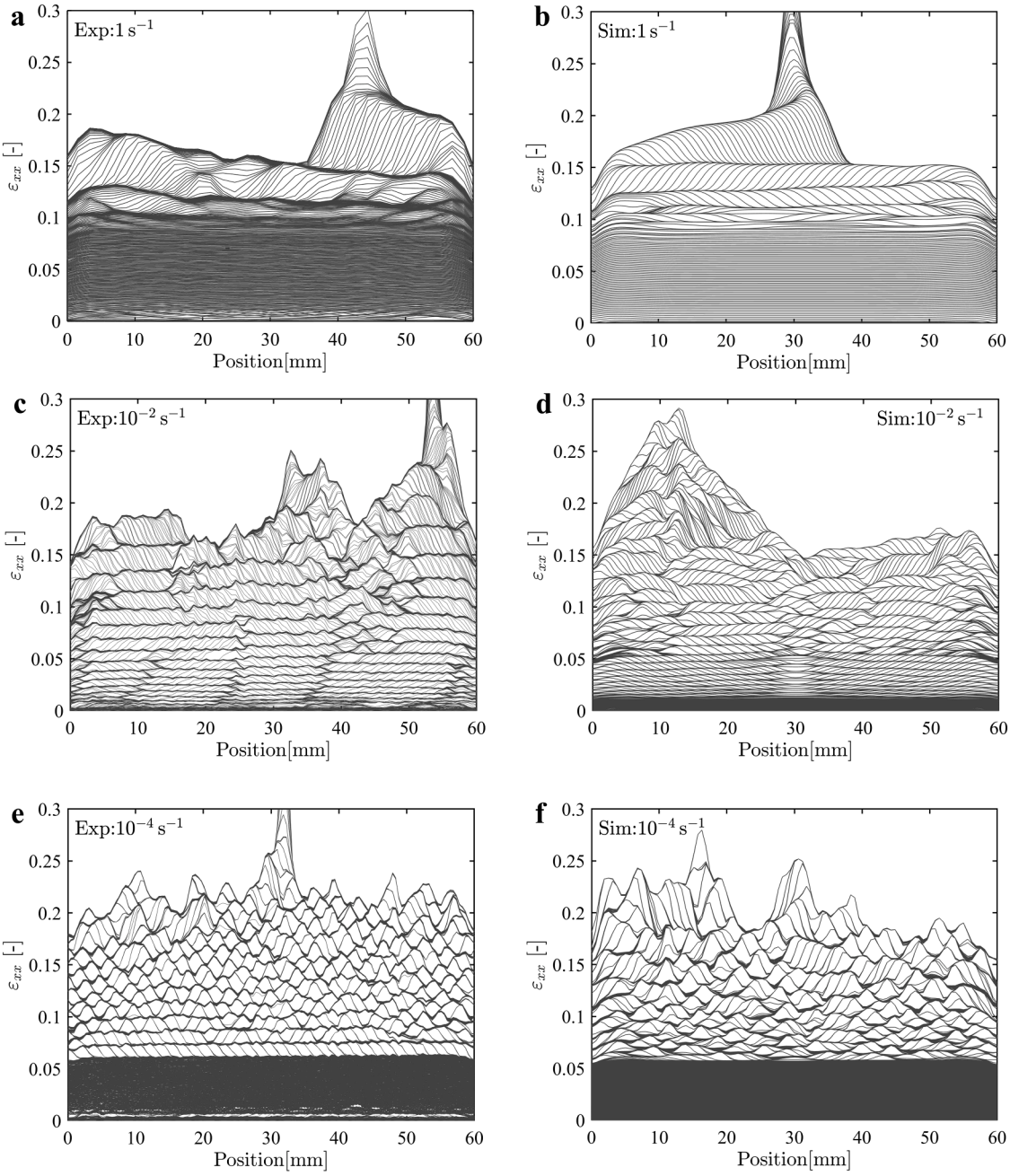

Fig. 10. Experimental and simulated throughout-test strain distributions along the centreline of the gauge length at different strain rates: Experiment: (a) $1s^{-1}$; (c) $10^{-2}s^{-1}$; (e) $10^{-4}s^{-1}$. Simulation: (b) $1s^{-1}$; (d) $10^{-2}s^{-1}$; (f) $10^{-4}s^{-1}$.

sequence of bands seems to be continuously propagating. However, a closer look at the DIC results reveals that the bands are discontinuous. Overall, the band is more randomly nucleated and non-propagating, which is a typical manifestation of type C band behaviour.

4.2. Heterogeneity of the strain field

The strain accumulation associated with the PLC effect is one of the most intriguing and unique features compared to normal deformation behaviour. The plasticity increment behaves like a moving or hopping "brush" painting the whole specimen. Due to the different spatially and temporally distributed PLC bands, the mode of strain accumulation also varies for different applied strain rates. The strain accumulation in both experiment and simulation is shown in Fig. 10. The lines in each figure refer to the strain distribution profiles along the centreline of the gauge length at all time instants.

At high strain rates, e.g., $1s^{-1}$ in Fig. 10a, the strain is evenly distributed before the onset of the PLC effect. Once the instability starts, a local strain accumulation will occur. The strain accumulation is quite random and weak in the beginning but becomes continuous and stronger afterwards. This is well captured by the simulation in Fig. 10b. The experimental result is less ordered compared to the model predictions, which again is due to the heterogeneity of the real material. In the later stage of deformation ($\varepsilon_{xx} > 0.15$), a well-defined band spreads across the specimen before necking. The neck occurs where the PLC band loses its mobility. This is in accordance with a previous study (Zhemchuzhnikova et al., 2018) and well reproduced by the simulation. For the tests at the intermediate strain rates, e.g., $10^{-2}s^{-1}$, an obvious difference is seen compared to the one at $1s^{-1}$. In the early stage of deformation, the specimen seems to be divided into several "segments". Within each segment, the strain accumulates continuously. This agrees with the short-distance propagating type B band behaviour. As the global strain increases, the segments becomes smaller and the strain accumulation site becomes more random, as seen in both experiment (Fig. 10c) and simulation (Fig. 10d). The experimental and simulated strain profiles for the test at low strain rate, e.g., $10^{-4}s^{-1}$, are shown in Fig. 10e and Fig. 10f, respectively. The bands are non-propagating, and the strain accumulation profile throughout the test looks like a "fish-scale". The hopping band accumulates the strain in a disordered manner. The position of the neck seems quite random and less correlated with the previous PLC bands compared to the high-rate test at $1s^{-1}$.

Fig. 11a shows an enlarged view of Fig. 10c (i.e., the test at $10^{-2}s^{-1}$) at the early stage of deformation around 0.3s~1.1 s. Before the PLC band appears, the deformation is quite uniform, however, there still exist some light fluctuations (highlighted by the black line) that are likely due to the initial roughness or microstructure heterogeneity of the specimen. It should be noted that the DIC noise might also contribute to this unevenness, especially during the initial stage of deformation. Then, four regions become simultaneously localized as shown in the figure. A non-uniform strain distribution is thus being built up at 0.92 s, denoted by the blue line. The strain valleys will be the favoured sites for the subsequent nucleation of PLC bands.

Fig. 11b shows the strain accumulation behaviour around 4.6 s ~ 6 s. A strain increment will be left behind in locations swept by the

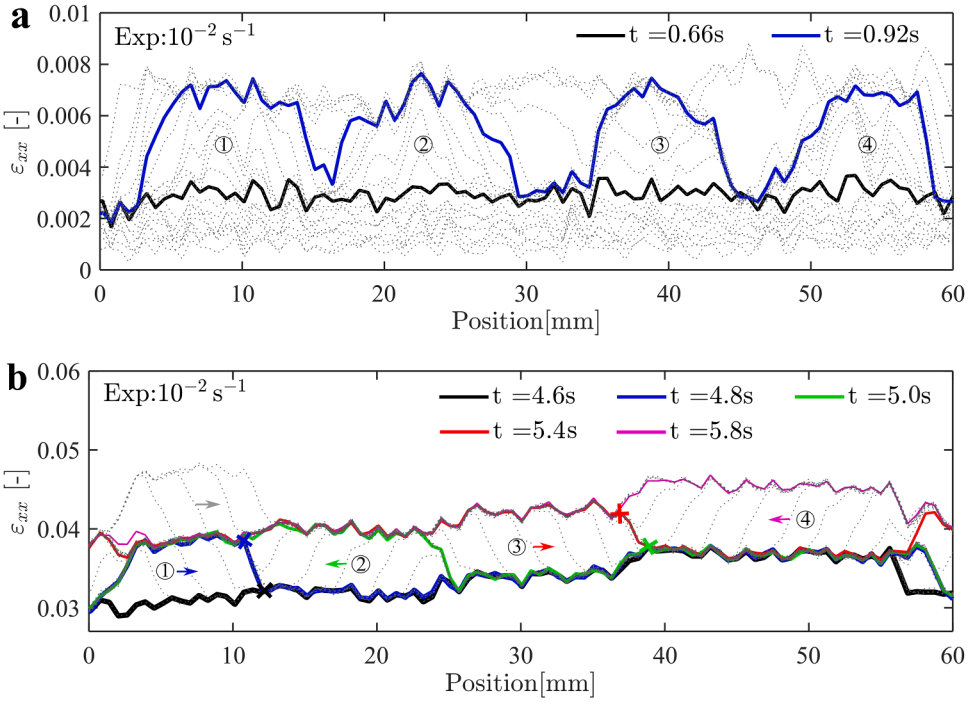

Fig. 11. Zoom-in of the strain accumulation process at $10^{-2}s^{-1}$ in Fig. 10c: (a) 0.3 s ~ 1.1 s, (b) 4.6 s ~ 6 s.

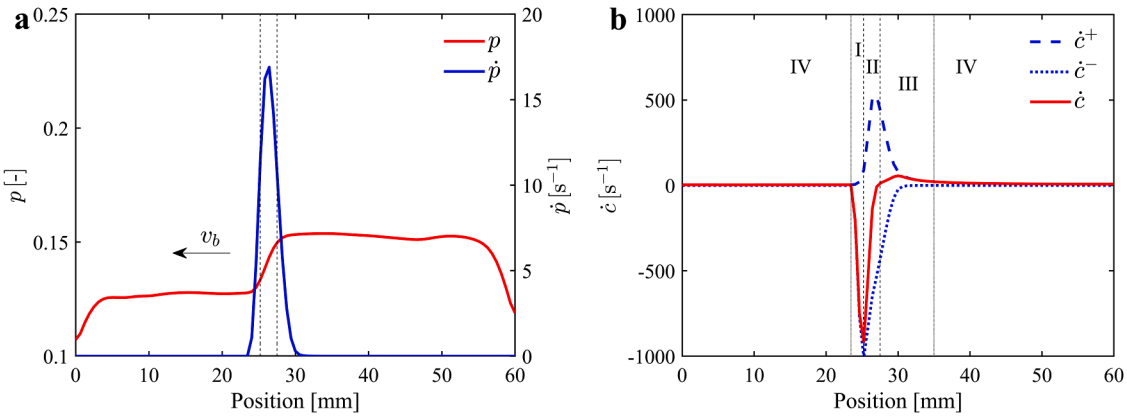

Fig. 12. (a) Simulated strain and strain rate distribution across the specimen at $t = 0.189$s for the test at $1s^{-1}$, and (b) rate of change of the solute concentration across the specimen together with the corresponding decomposed solute pinning and unpinning rate.

PLC band front. The solid lines represent the as-built strain state at five different given time instants. Four regions are illustrated in the figure to show the separate segments of band propagation. At $t = 4.6$s, the corresponding strain distribution across the specimen is denoted by the black lowermost line. Afterwards, a band is nucleated to the left of region ① and moves towards the right side until it meets a local strain peak, which is shown by the cross-symbol in black. At $t = 4.8$ s,a band nucleates in the right part of region ②, This band moves towards the left side until it encounters the edge of the previous strain "hill" denoted by the cross-symbol in blue. This process of band nucleation and short movements will repeat itself with continuing deformation. From this detailed inspection of the strain accumulation process, it is obvious that the former strain profile exerts a strong influence on the subsequent band nucleation and propagation. The strain gradient around the edge of the band front inherently creates a roughness of the specimen.

4.3. Detailed analysis of strain ageing

A unique feature associated with the PLC effect is that the state of the material will keep changing as the deformation proceeds. Inside the band, the moving dislocations are repeatedly caught and released by dynamic strain ageing (DSA). The material outside the band, although in the elastic state, experiences the ageing effect as well. This resembles the static strain ageing (SSA) process that is usually associated with the Lüders phenomenon. In this section, we will investigate the ageing process both inside and outside the PLC band.

Outside the PLC band, the material is in the elastic state. The corresponding steady-state ageing time $t_{a,ss}$ will approach infinity due to the vanishing of the plastic strain rate $\dot{p}$, i.e., $t_{a,ss} = \frac{\Omega}{\dot{p}} \to \infty$. Hähner (1996) questioned the underlying physics of McCormick's model. However, in the current FE simulations, the material in the elastic state does not depend on the solution from $t_{a,ss} = \frac{\Omega}{\dot{p}}$. Instead, the relaxation function is applied also during the static strain ageing when the material is elastically loaded, for which $t_{a,ss}$ becomes very large, and hence $\dot{t}_a \approx 1$, according to Eq. (12), i.e. $dt_a \approx dt$ and ageing time outside the band evolves with the "real" time increment. This approach solves the singularity issue as pointed by Hähner (1996). Hence, at any sites outside the band, the ageing time t_a will keep on increasing during the test. Inside the PLC band, the material is in the plastic state, and McCormick's relaxation function, defined by Eq. (14), is used to describe the ageing time evolution both in the steady and non-steady state.

After obtaining the ageing time, the corresponding solute concentration both inside and outside the PLC band will be calculated based on Eq. (10). The relative effective solute concentration can be expressed by the ageing time as

$$c(t_a) = 1 - \exp\left(- \left(\frac{t_a}{t_d}\right)^n \right) \tag{15}$$

By differentiating Eq. (15) with respect to time, we get

$$\dot{c} = \dot{c}^+ + \dot{c}^-$$

$$\dot{c}^- = \frac{n(1-c)(-\ln(1-c))^{\frac{n-1}{n}}}{t_d}$$

$$\dot{c}^+ = -\frac{n(1-c)\ln(1-c)}{t_{a,ss}} \tag{16}$$

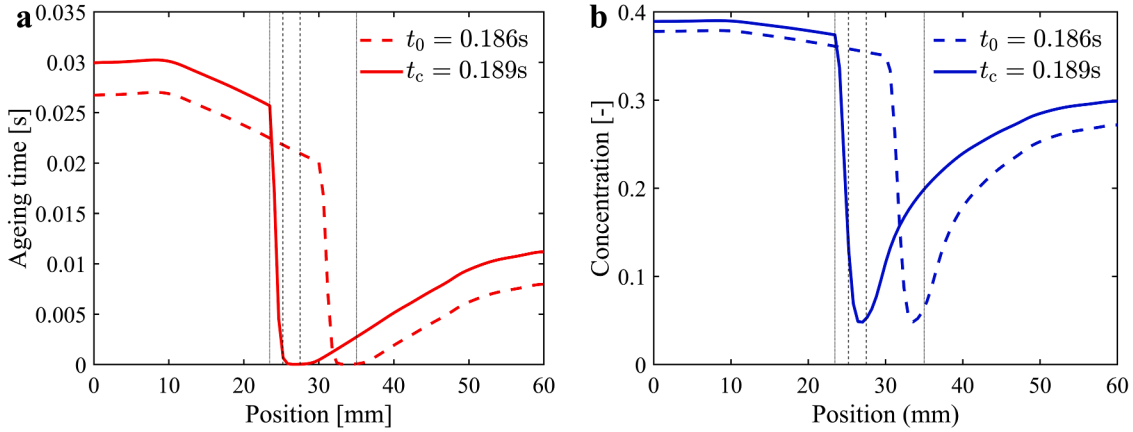

Fig. 13. Simulated (a) ageing time and (b) relative effective solute concentration distributions across the specimen for the test at $1s^{-1}$ at 0.186 s (previous state) and 0.189 s (current state corresponds to Fig. 12).

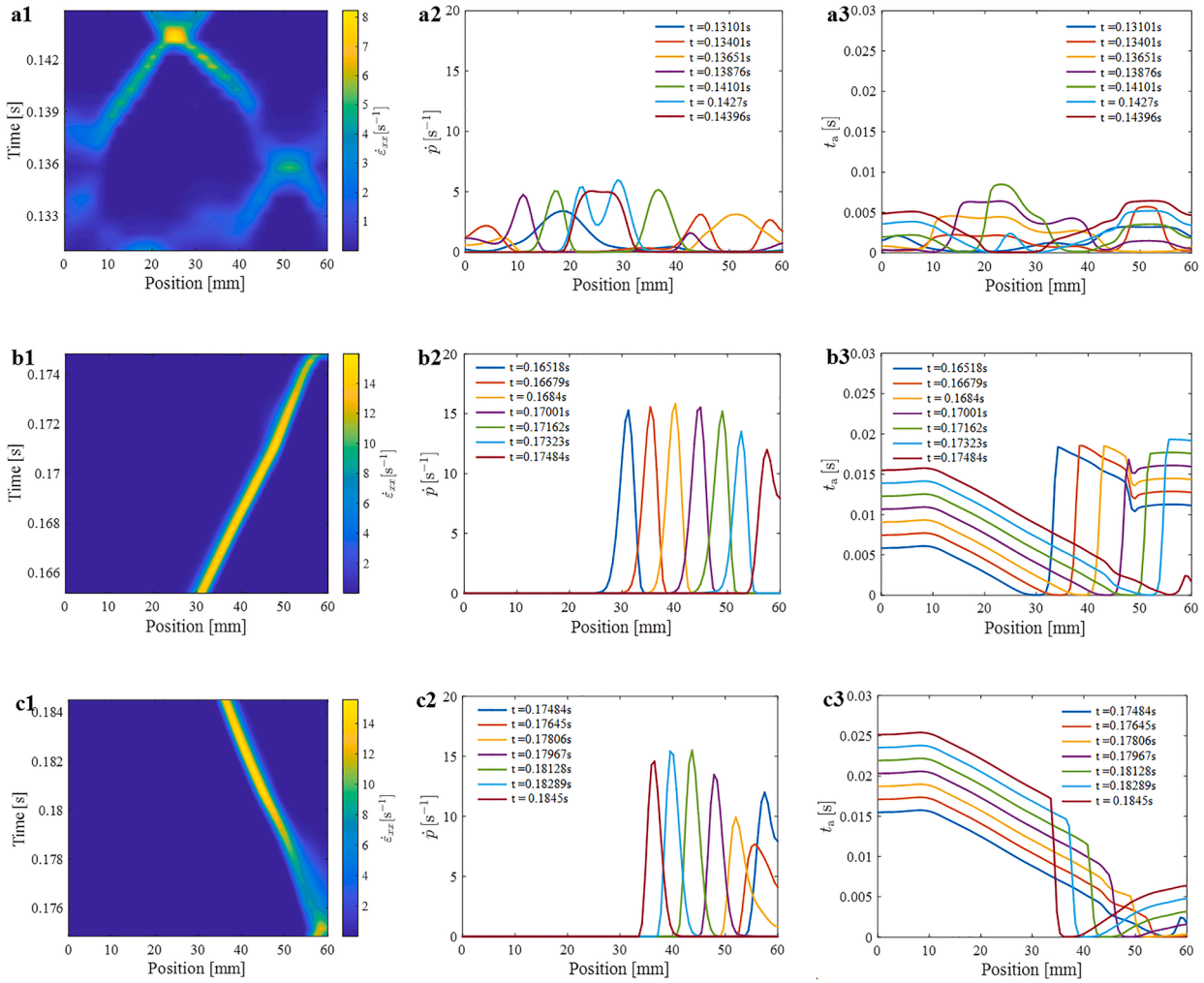

Fig. 14. Simulated spatio-temporal pattern and the corresponding plastic rate and ageing time distribution along the gauge length for the test at $1s^{-1}$: (a1-a3) 0.131s-0.144 s; (b1-b3) 0.165–0.175 s; (c1-c3) 0.175s-0.185 s.

where $\dot{c}$ is rate of change of the solute concentration; $\dot{c}^+$ is the positive part of $\dot{c}$, which represents the solute pinning rate, and $\dot{c}^-$ is the negative part of $\dot{c}$, which represents the unpinning rate. Similar decomposition can be found in Rizzi and Hähner (2004) and Jiang et al. (2007). In the work of Rizzi and Hähner (2004), this decomposition is done in terms of the additional activation enthalpy brought by solute diffusion. As is well known, the PLC effect usually appears when the solute diffusion and the dislocation arrest have comparable time scales. An interplay between the solute pinning and unpinning process will lead to the discontinuous plastic flow. In order to accurately investigate this behaviour, $\dot{c}^+$ and $\dot{c}^-$ are then included as the solution dependant variables (SDVs) in the user material subroutine according to Eq. (16).

In the following, the ageing process will be discussed in detail. The simulation results for the test at the strain rate of $1\mathrm{s}^{-1}$ will be used as an illustrative example. In Fig. 12a, a band continuously propagates from the right side towards the left side. The region that is already swept by the band shows a higher strain accumulation than the sites in front of the band, see the red line. The hill-like strain rate profile in blue denotes the current position of the PLC band. The dashed lines in black delimit the centre of the PLC band and corresponds to region II in Fig. 12b, which shows the rate of change of the solute concentration across the specimen. The blue dashed and dotted lines represent the pinning rate $\dot{c}^+$ and unpinning rate $\dot{c}^-$, respectively. It is seen that only the places nearby the PLC band front experience significant pinning and unpinning rate due to DSA. The sum of these two rates gives the net rate of change of the solute concentration $\dot{c}$. Four distinct regions can be seen: region I is about to be swept by the PLC band and the dislocations become unpinned from the solute clouds ($\dot{c} < 0$); region II is currently inside the band centre with rapid dislocation glide ($\dot{c} < 0$); region III has just been swept by the PLC band and dislocations become recaptured and pinned ($\dot{c} > 0$); and region IV is outside the band and the dislocations remains arrested ($\dot{c}$ is small). The simulation result agrees quite well with the physical interpretations within the PLC band propagation process given by Rizzi and Hähner (2004).

Fig. 13 shows the current ageing time and solute concentration distributions across the specimen corresponding to the state in Fig. 12 at 0.189 s. For a better illustration, the lines representing the different regions in Fig. 12b are kept. A previous state at 0.186 s is also plotted in the same figure to show the evolution of the ageing time and the solute concentration. The band moves continuously during the time interval between 0.186 s and 0.189 s. In front of the PLC band (roughly within 0~25 mm) in Fig. 13a, it is seen that the ageing time increases with the real time increment. The corresponding effective solute concentration increases as well based on Eq. (15), see Fig. 13b. Within the adjacent area of the PLC band front (25~35 mm), the ageing time for the previous state is reset to a small value. This is because the high local plastic strain rate for the test at $1\mathrm{s}^{-1}$ results in a very limited time for dynamic strain ageing. Interestingly, the area that has already been swept by the PLC band (35~60 mm) again shows a higher ageing time. The material becomes aged again due to the SSA effect as mentioned above.

By taking the strain ageing process both inside and outside the PLC band into account, we will in the following investigate the influence of strain ageing on the spatio-temporal behaviour of the band. As already shown, different spatio-temporal patterns will be generated at different applied strain rates. However, there is no essential difference between the different spatio-temporal patterns with regards to the strain ageing process. For a better illustration, we will again take the simulated test at $1\mathrm{s}^{-1}$ as an example due to its relatively ordered characteristics.

In the early stage of deformation, the band is quite weak along with relatively random nucleation, see Fig. 14-a. The ageing time appears irregular as well, due to the recurrent change of the band position. With the formation of a well-defined PLC band, a single type A band propagates continuously shown in Fig. 14-b1. The hill-like strain rate peak also moves towards the right grip end in Fig. 14-b2. As discussed above, the ageing time increases by SSA outside the PLC band and is governed by DSA inside the PLC band. Special attention should be paid to the state at $t = 0.17484\mathrm{s}$, where the band hits the right grip end of the specimen. At this particular time, the specimen has just been traversed by the PLC band and all sites have approximately the same strain accumulation. However, an ageing time gradient is left behind at this moment, see Fig. 14-b3. The position with the least ageing time and thus the lowest solute strengthening will be a favourable site for the next band nucleation. Hence, the PLC band in this case hits and reflects around the grip end. Afterwards, the same process will repeat until the end of deformation in Fig. 14-c.

4.4. *Combined effects of strain heterogeneity and strain ageing*

The spatio-temporal behaviour of the PLC bands varies with the applied strain rate. Both the strain accumulation and the strain ageing are important for the band nucleation and propagation. The material work hardens due to the strain brought by the PLC band. Meanwhile, the solute diffusion both inside and outside the PLC band changes the state of the material. The combined influence of work hardening and strain ageing on the spatio-temporal patterns will be considered in this section.

Fig. 15 shows the simulated stress distributions at two given time instants for the test at $1\mathrm{s}^{-1}$. The plastic strain distributions, as seen in Fig. 10a, and the ageing-time distributions, similar as the example in Fig. 13, result in the non-uniform distributions of the work hardening stress R and the ageing stress σ_a, respectively. According to Eq. (3), the sum of these two stress contributions equals the current yield stress, excluding its initial constant value σ_0. A local yield stress minimum is observed both in Fig. 15a and Fig. 15b. The PLC band will nucleate uniquely in these favourable sites.

A continuously moving band will thus appear. The work hardening and ageing contributions for the test at $10^{-2}\mathrm{s}^{-1}$ in Fig. 16 are displayed in the same way as in Fig. 15. However, in this case it is found that several local yield stress minima occur simultaneously. The PLC band in this case shows a more random nucleation.

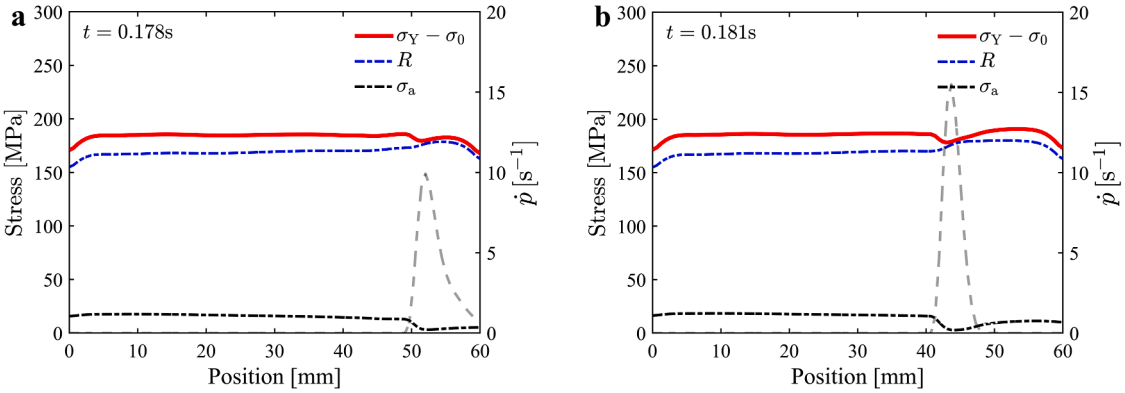

Fig. 15. Simulated stress distribution across the specimen for a continuously propagating band scenario at 1s^{-1}: (a) $t = 0.178$s and (b) $t = 0.181$s. The corresponding strain rate profile is also included with grey dashed lines in the same figure, with the corresponding axis on the right-hand side of the figure.

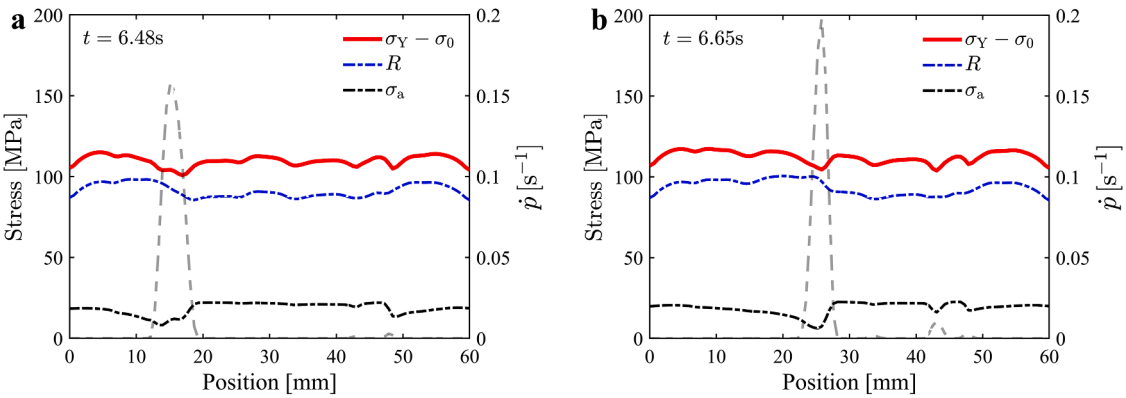

Fig. 16. Simulated stress distribution across the specimen for a hopping band scenario at 10^{-2}s^{-1}: (a) $t = 6.48$s and (b) $t = 6.65$s. The corresponding strain rate profile is also included in the same figure.

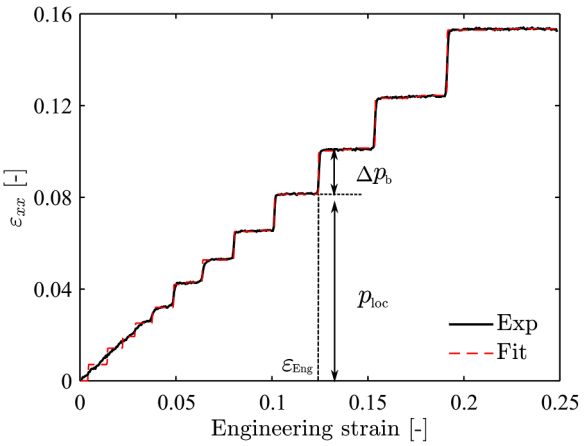

Fig. 17. Illustration of the analysis method for determining the band strain.

4.5. PLC band characteristics

The band strain is usually manually measured from the height of the band strain profile and the velocity of the band can be calculated from the slope of continuous portion of the spatio-temporal patterns measured by DIC in Fig. 3. However, due to the uncertainty of an individual band event, the acquired data may exhibit some randomness and deviate from the reality. Besides, this approach results in the scarcity of data points for subsequent systematic analysis. A newly developed method from our previous work is utilized here to track the PLC band characteristics (Xu et al., 2023) . Firstly, the staircase-like strain history from all the points across the extensometer is exported from the DIC. Then, a function consisting of a sum of Heaviside step-functions, is used to fit the strain history curve of each individual point, see Fig. 17. Once the curve has been fitted, three key parameters associated with the PLC band event can be obtained. The band strain Δp_b equals the height of the strain step. The corresponding time instant or engineering strain for the band event is represented by the abscissa of the strain step. In addition, the accumulated "local" strain p_{loc} before each individual band event is also extracted. Details of this method can be referred to Xu et al. (2023).

Fig. 18 shows the experimental band strain Δp_b for all time instants throughout the test. It is clearly seen that the band strain increases with the global strain. After 20% strain, the band strain exhibits a significant increase, which is because the material is quite close to necking. After obtaining the band strain, the band velocity v_b can be calculated (Rizzi and Hähner, 2004; Xu et al., 2023), as

$$v_b = \frac{v_g}{\Delta p_b} \tag{17}$$

where the elongation speed of the virtual extensometer v_g can be directly obtained from the DIC measurements. It is approximately equal to 4.36 mm/s for the test at $10^{-1}s^{-1}$. The band velocity v_b shows a decrease with the global strain in Fig. 18b.

The band behaviour is governed by the constitutive relation in Eq. (8). As shown for a continuously propagating band in Fig. 15, inside the band, the local high strain rate will bring a higher viscous stress than elsewhere. While in front of the band, where the strain and thus the work-hardening is less than behind the band, the equilibrium stress is achieved by the contribution to the flow stress from

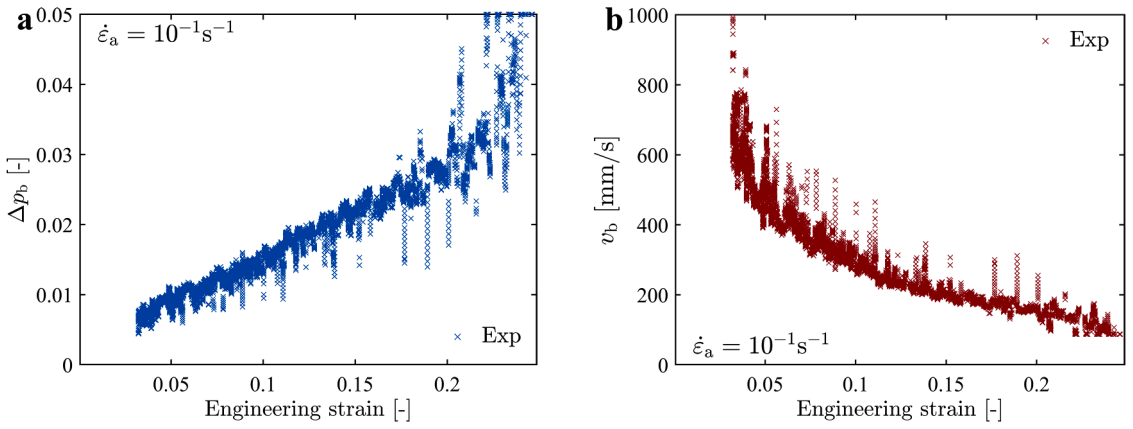

Fig. 18. Experimental (a) band strain Δp_b and (b) band velocity v_b for the test at $10^{-1}s^{-1}$.

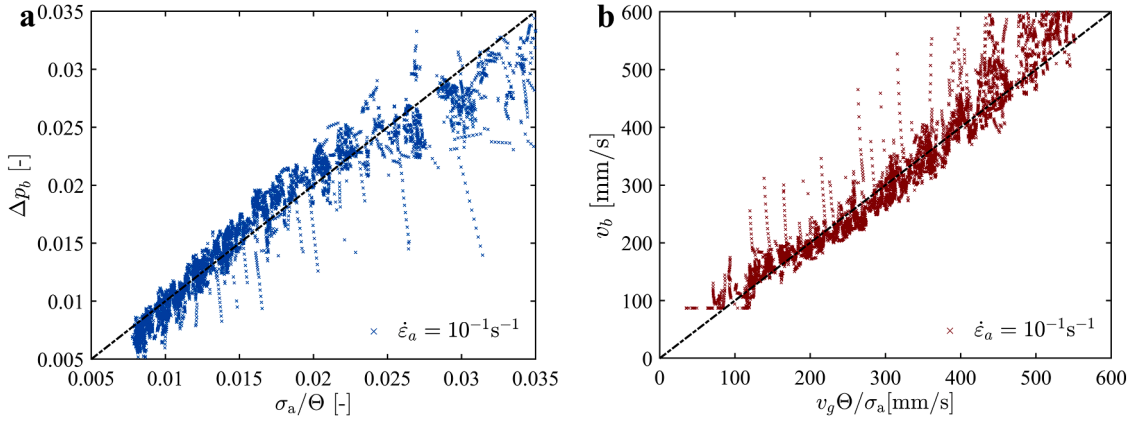

Fig. 19. (a) Experimental (×) and theoretical (dashed line) band strain Δp_b plotted against σ_a/Θ, and (b) experimental (×) and theoretical (dashed line) band velocity v_b plotted against $v_g\Theta/\sigma_a$ for the test at $10^{-1}s^{-1}$.

DSA, i.e.,

$$\sigma_a \approx R(\Delta p_b) \approx \Theta \Delta p_b \tag{18}$$

Here Θ is the current work hardening rate for a given microstructure, which can be expressed as

$$\Theta = \Theta_0 \exp\left(-\frac{p}{p_0}\right) \tag{19}$$

According to Eq. (9), we have $\Theta_0 = C_R Q_R$ and $p_0 = 1/C_R$. Combining Eq. (18) and Eq. (20), the final expression for the band strain becomes

$$\Delta p_b = \sigma_a \Big/ \Theta = \frac{\sigma_a}{\Theta_0} \exp\left(\frac{p}{p_0}\right) \tag{20}$$

This equation indicates that band strain is strongly dependant on the work hardening behaviour of the material.
With Eq. (17) and Eq. (20), the band velocity becomes

$$v_b = \frac{v_g \Theta}{\sigma_a} = \frac{\Theta_0}{\sigma_a} v_g \exp\left(-\frac{p}{p_0}\right) \tag{21}$$

The band velocity increases with the gauge elongation speed v_g, which is reasonable, since the band has to transverse the specimen to accommodate the applied (global) strain rate. The work hardening rate of the material plays a role in the band velocity as well. As the deformation proceeds, the lowering of the work hardening rate results in a decrease of the band velocity. A recently published lower-scale study (Mäkinen et al., 2020), based on the PLC-related dislocation avalanches, concludes with a very similar expression as in Eq. (21) for the band velocity.

By measuring band strains and velocities from the DIC measurements, as described above, it is possible to check if the estimates by Eq. (20) and Eq. (21) are correct. In Fig. 19a, the band strain Δp_b, taken from the data shown in Fig. 18a, is compared to the theoretically calculated band strain by Eq. (20). Since the solute strengthening is overestimated by the current model, therefore, instead of using σ_{a0} in Eq. (11), the ageing stress σ_a is assumed to be equal to 15 MPa. This value corresponds to the magnitude of the serration amplitude from experiment at 10^{-4} s^{-1} as shown in Fig. 7e, in which case the force is fully unloaded and is therefore used as a rough estimate of the ageing stress contribution. In Eq. (20), the parameters Θ_0 and p_0 are calculated from the identified C_R and Q_R, to roughly estimate the work hardening rate Θ. The plastic strain p in Eq. (20) is set equal to the local accumulated strain p_{loc} before each individual band event. As shown in Fig. 19a, a strong correlation is found between measured and theoretical Δp_b. A similar plot of the band velocity v_b as a function of $v_g \Theta/\sigma_a$ is presented in Fig. 19b, and again a strong correlation is found, which supports the validity of Eq. (21).

5. Conclusions

In this work, the Portevin–Le Chatelier (PLC) effect in an AlMg alloy (AA5182-O) is investigated. Direct observations using digital image correlation (DIC) provide a thorough detailed description of the influence of strain rate on the serration morphologies, the critical strain, the spatio-temporal patterns and the band characteristics, and serve as a basis for comparison with finite element (FE) simulations. The conclusions are the following:

- The modified Kubin-Estrin-McCormick (KEMC) model which assumes a strain dependant saturation ageing stress (Böhlke et al., 2009), is able to reproduce the stress differences and the serration morphologies at the different applied strain rates, while the model overestimates the serration amplitudes.
- By employing an ultra-high DIC image acquisition frequency focused on the limited image area of the specimen, we were able to observe both the normal and inverse critical strain behaviours in the AA5182-O alloy at room temperature. As the strain rates increased, we could discern the details of the transition from discontinuous to continuous propagation of PLC bands.
- Detailed analysis of the spatio-temporal patterns reveals how the nucleation and propagation of the PLC bands are influenced by the as-built strain accumulation and the ageing process. Insight into the detailed solute pinning and unpinning processes along with the band movement are gained from the detailed FE simulations. Formation of distinct or multiple local yield stress minima account for the band propagating or hopping characteristics.
- By accurate and efficient band characteristic measurements, the band strain is found to mainly depend on the material properties, i.e., the work-hardening rate and the solute strengthening, while the band velocity is found to be influenced not only apparently by the applied strain rate but more by the material properties.
- The spatio-temporal patterns and the strain accumulation processes measured by DIC, is well captured by the corresponding FE simulations. The detailed analysis in this work of how the mechanisms relates to the measured and simulated complex PLC behaviour, may shed new light on many existing experimental works on the PLC band characteristics.

CRediT authorship contribution statement

Jianbin Xu: Investigation, Conceptualization, Methodology, Software, Formal analysis, Writing – original draft. **Odd Sture**

Hopperstad: Conceptualization, Supervision, Funding acquisition, Writing – review & editing. **Bjørn Holmedal:** Conceptualization, Supervision, Writing – review & editing. **Torodd Berstad:** Methodology, Software. **Tomáš Mánik:** Conceptualization, Supervision, Writing – review & editing. **Knut Marthinsen:** Conceptualization, Supervision, Funding acquisition, Project administration, Writing – review & editing.

Declaration of Competing Interest

The authors declare that they have no known competing financial interests or personal relationships that could have appeared to influence the work reported in this paper.

Data availability

No data was used for the research described in the article.

Acknowledgements

This research was conducted at the Centre for Advanced Structural Analysis (CASA), funded by the Research Council of Norway [grant number 237885] and several public and company partners.

References

Ait-Amokhtar, H., Fressengeas, C., 2010. Crossover from continuous to discontinuous propagation in the Portevin–Le Chatelier effect. Acta Mater. 58, 1342–1349.
Ait-Amokhtar, H., Vacher, P., Boudrahem, S., 2006. Kinematics fields and spatial activity of Portevin–Le Chatelier bands using the digital image correlation method. Acta Mater. 54, 4365–4371.
Belytschko, T., Liu, W.K., Moran, B., Elkhodary, K., 2013. Nonlinear Finite Elements For Continua and Structures. John wiley & sons.
Benallal, A., Berstad, T., Børvik, T., Clausen, A., Hopperstad, O., 2006. Dynamic strain aging and related instabilities: experimental, theoretical and numerical aspects. Eur. J. Mech. A Solids 25, 397–424.
Benallal, A., Berstad, T., Børvik, T., Hopperstad, O.S., Koutiri, I., de Codes, R.N., 2008a. An experimental and numerical investigation of the behaviour of AA5083 aluminium alloy in presence of the Portevin–Le Chatelier effect. Int. J. Plast. 24, 1916–1945.
Benallal, A., Berstad, T., Børvik, T., Hopperstad, O.S., Nogueira de Codes, R., 2008b. Effects of strain rate on the characteristics of PLC deformation bands for AA5083-H116 aluminium alloy. Philos. Mag. 88, 3311–3338.
Besnard, G., Hild, F., Roux, S., 2006. Finite-element" displacement fields analysis from digital images: application to Portevin–Le Châtelier bands. Exp. Mech. 46, 789–803.
Böhlke, T., Bondár, G., Estrin, Y., Lebyodkin, M., 2009. Geometrically non-linear modeling of the Portevin–Le Chatelier effect. Comput. Mater. Sci. 44, 1076–1088.
Chen, H., Chen, Z., Ji, G., Zhong, S., Wang, H., Borbély, A., Ke, Y., Bréchet, Y., 2021. The influence of shearable and nonshearable precipitates on the Portevin-Le Chatelier behavior in precipitation hardening AlMgScZr alloys. Int. J. Plast. 147, 103120.
Cottrell, A.H., Bilby, B., 1949. Dislocation theory of yielding and strain ageing of iron. Proc. Phys. Soc. London Sect. A 62, 49.
De Codes, R.N., Hopperstad, O., Engler, O., Lademo, O.G., Embury, J., Benallal, A., 2011. Spatial and temporal characteristics of propagating deformation bands in AA5182 alloy at room temperature. Metall. Mater. Trans. A 42, 3358–3369.
Fagerholt, E., 2012. Field measurements in mechanical testing using close-range photogrammetry and digital image analysis.
Fu, S., Cheng, T., Zhang, Q., Hu, Q., Cao, P., 2012. Two mechanisms for the normal and inverse behaviors of the critical strain for the Portevin–Le Chatelier effect. Acta Mater. 60, 6650–6656.
Hähner, P., 1996. On the physics of the Portevin-Le Châtelier effect part 1: the statistics of dynamic strain ageing. Mater. Sci. Eng. A 207, 208–215.
Hähner, P., Rizzi, E., 2003. On the kinematics of Portevin–Le Chatelier bands: theoretical and numerical modelling. Acta Mater. 51, 3385–3397.
Hähner, P., Ziegenbein, A., Rizzi, E., Neuhäuser, H., 2002. Spatiotemporal analysis of Portevin–Le Châtelier deformation bands: theory, simulation, and experiment. Phys. Rev. B 65, 134109.
Halim, H., Wilkinson, D.S., Niewczas, M., 2007. The Portevin–Le Chatelier (PLC) effect and shear band formation in an AA5754 alloy. Acta Mater. 55, 4151–4160.
Hallai, J.F., Kyriakides, S., 2013. Underlying material response for Lüders-like instabilities. Int. J. Plast. 47, 1–12.
Hopperstad, O., Børvik, T., Berstad, T., Lademo, O., Benallal, A., 2007. A numerical study on the influence of the Portevin–Le Chatelier effect on necking in an aluminium alloy. Modell. Simul. Mater. Sci. Eng. 15, 747.
Jacobs, T.R., Matlock, D.K., Findley, K.O., 2019. Characterization of localized plastic deformation behaviors associated with dynamic strain aging in pipeline steels using digital image correlation. Int. J. Plast. 123, 70–85.
Jiang, H., Zhang, Q., Chen, X., Chen, Z., Jiang, Z., Wu, X., Fan, J., 2007. Three types of Portevin–Le Chatelier effects: experiment and modelling. Acta Mater. 55, 2219–2228.
Kabirian, F., Khan, A.S., Pandey, A., 2014. Negative to positive strain rate sensitivity in 5xxx series aluminum alloys: experiment and constitutive modeling. Int. J. Plast. 55, 232–246.
Kang, J., Mishra, R.K., Wilkinson, D.S., Hopperstad, O.S., 2012. Effect of Mg content on Portevin–Le Chatelier band strain in Al–Mg sheet alloys. Philos Mag Lett 92, 647–655.
Klusemann, B., Fischer, G., Böhlke, T., Svendsen, B., 2015. Thermomechanical characterization of Portevin–Le Châtelier bands in AlMg3 (AA5754) and modeling based on a modified Estrin–McCormick approach. Int. J. Plast. 67, 192–216.
Kobelev, N.P., Lebyodkin, M.A., Lebedkina, T.A., 2017. Role of self-organization of dislocations in the onset and kinetics of macroscopic plastic instability. Metall. Mater. Trans. A 48, 965–974.
Kubin, L., Estrin, Y., 1990. Evolution of dislocation densities and the critical conditions for the Portevin-Le Chatelier effect. Acta Metall. Mater. 38, 697–708.
Kubin, L., Fressengeas, C., Ananthakrishna, G., 2002. Collective Behaviour of Dislocations in plasticity, Dislocations in Solids. Elsevier, pp. 101–192.
Lebyodkin, M., Dunin-Barkowskii, L., Brechet, Y., Estrin, Y., Kubin, L., 2000. Spatio-temporal dynamics of the Portevin–Le Chatelier effect: experiment and modelling. Acta Mater. 48, 2529–2541.
Lee, S.Y., Takushima, C., Hamada, J.-i., Nakada, N., 2021. Macroscopic and microscopic characterizations of Portevin-LeChatelier effect in austenitic stainless steel using high-temperature digital image correlation analysis. Acta Mater. 205, 116560.
Li, X., Roth, C.C., Mohr, D., 2019. Machine-learning based temperature-and rate-dependent plasticity model: application to analysis of fracture experiments on DP steel. Int. J. Plast. 118, 320–344.
Louat, N., 1981. On the theory of the Portevin-Le Chatelier effect. Scr. Metall. 15, 1167–1170.

Luo, S., Castany, P., Thuillier, S., Huot, M., 2018. Spatiotemporal characteristics of Portevin-Le Chatelier effect in Ti-Mo alloys under thermo-mechanical loading. Mater. Sci. Eng. A 733, 137–143.
Mäkinen, T., Karppinen, P., Ovaska, M., Laurson, L., Alava, M.J., 2020. Propagating bands of plastic deformation in a metal alloy as critical avalanches. Sci Adv 6, eabc7350.
Manach, P.Y., Thuillier, S., Yoon, J.W., Coër, J., Laurent, H., 2014. Kinematics of Portevin–Le Chatelier bands in simple shear. Int. J. Plast. 58, 66–83.
Marais, A., Mazière, M., Forest, S., Parrot, A., Le Delliou, P., 2012. Identification of a strain-aging model accounting for Lüders behavior in a C-Mn steel. Philos. Mag. 92, 3589–3617.
Mazière, M., Besson, J., Forest, S., Tanguy, B., Chalons, H., Vogel, F., 2010. Numerical aspects in the finite element simulation of the Portevin–Le Chatelier effect. Comput. Methods Appl. Mech. Eng. 199, 734–754.
Mazière, M., Dierke, H., 2012. Investigations on the Portevin Le Chatelier critical strain in an aluminum alloy. Comput. Mater. Sci. 52, 68–72.
McCormick, P., 1988. Theory of flow localisation due to dynamic strain ageing. Acta Metall. 36, 3061–3067.
McCormick, P., Ling, C., 1995. Numerical modelling of the Portevin—Le Chatelier effect. Acta Metall. Mater. 43, 1969–1977.
Min, J., Hector Jr, .L..G.., Lin, .J.., Carter, .J..T.., Sachdev, A.K., 2014. Spatio-temporal characteristics of propagative plastic instabilities in a rare earth containing magnesium alloy. Int. J. Plast. 57, 52–76.
Mulford, R., Kocks, U., 1979. New observations on the mechanisms of dynamic strain aging and of jerky flow. Acta Metall. 27, 1125–1134.
Penning, P., 1972. Mathematics of the portevin-le chatelier effect. Acta Metall. 20, 1169–1175.
Ranc, N., Wagner, D., 2005. Some aspects of Portevin–Le Chatelier plastic instabilities investigated by infrared pyrometry. Mater. Sci. Eng. A 394, 87–95.
Ren, S., Mazière, M., Forest, S., Morgeneyer, T.F., Rousselier, G., 2017. A constitutive model accounting for strain ageing effects on work-hardening. Application to a C–Mn steel. Comptes Rendus Mécanique 345, 908–921.
Ren, S.C., Morgeneyer, T.F., Mazière, M., Forest, S., Rousselier, G., 2021. Effect of Lüders and Portevin–Le Chatelier localization bands on plasticity and fracture of notched steel specimens studied by DIC and FE simulations. Int. J. Plast. 136, 102880.
Rizzi, E., Hähner, P., 2004. On the Portevin–Le Chatelier effect: theoretical modeling and numerical results. Int. J. Plast. 20, 121–165.
Shabadi, R., Kumar, S., Roven, H.J., Dwarakadasa, E., 2004. Characterisation of PLC band parameters using laser speckle technique. Mater. Sci. Eng. A 364, 140–150.
Shen, F., Münstermann, S., Lian, J., 2020. An evolving plasticity model considering anisotropy, thermal softening and dynamic strain aging. Int. J. Plast. 132, 102747.
Swaminathan, B., Abuzaid, W., Sehitoglu, H., Lambros, J., 2015. Investigation using digital image correlation of Portevin-Le Chatelier Effect in Hastelloy X under thermo-mechanical loading. Int. J. Plast. 64, 177–192.
Wang, J., Guo, W.G., Gao, X., Su, J., 2015. The third-type of strain aging and the constitutive modeling of a Q235B steel over a wide range of temperatures and strain rates. Int. J. Plast. 65, 85–107.
Wenman, M., Chard-Tuckey, P., 2010. Modelling and experimental characterisation of the Lüders strain in complex loaded ferritic steel compact tension specimens. Int. J. Plast. 26, 1013–1028.
Xu, J., Holmedal, B., Hopperstad, O.S., Maník, T., Marthinsen, K., 2022. Dynamic strain ageing in an AlMg alloy at different strain rates and temperatures: experiments and constitutive modelling. Int. J. Plast., 103215
Xu, J., Liu, L., Hopperstad, O.S., Holmedal, B., Mánik, T., Marthinsen, K., 2023. A simple method enabling efficient quantitative analysis of the Portevin–Le Chatelier band characteristics. Scr. Mater. 222, 115027.
Yang, F., Luo, H., Pu, E., Zhang, S., Dong, H., 2018. On the characteristics of Portevin–Le Chatelier bands in cold-rolled 7Mn steel showing transformation-induced plasticity. Int. J. Plast. 103, 188–202.
Yuzbekova, D., Mogucheva, A., Borisova, Y., Kaibyshev, R., 2021. On the mechanisms of nucleation and subsequent development of the PLC bands in an AlMg alloy. J. Alloys Compd. 868, 159135.
Yuzbekova, D., Mogucheva, A., Zhemchuzhnikova, D., Lebedkina, T., Lebyodkin, M., Kaibyshev, R., 2017. Effect of microstructure on continuous propagation of the Portevin–Le Chatelier deformation bands. Int. J. Plast. 96, 210–226.
Zavattieri, P., Savic, V., Hector Jr, L., Fekete, J., Tong, W., Xuan, Y., 2009. Spatio-temporal characteristics of the Portevin–Le Châtelier effect in austenitic steel with twinning induced plasticity. Int. J. Plast. 25, 2298–2330.
Zhang, Q., Jiang, Z., Jiang, H., Chen, Z., Wu, X., 2005. On the propagation and pulsation of Portevin-Le Chatelier deformation bands: an experimental study with digital speckle pattern metrology. Int. J. Plast. 21, 2150–2173.
Zhang, S., McCormick, P.G., Estrin, Y., 2001. The morphology of Portevin–Le Chatelier bands: finite element simulation for Al–Mg–Si. Acta Mater 49, 1087–1094.
Zhemchuzhnikova, D., Lebyodkin, M., Yuzbekova, D., Lebedkina, T., Mogucheva, A., Kaibyshev, R., 2018. Interrelation between the Portevin Le-Chatelier effect and necking in AlMg alloys. Int. J. Plast. 110, 95–109.